# Resistance and wake distortion optimization of JBC considering ship-propeller interaction

Zhiqiang Liu [a], Weiwen Zhao [a], Decheng Wan [a,b,*]

[a] *Computational Marine Hydrodynamics Lab (CMHL), School of Naval Architecture, Ocean and Civil Engineering, Shanghai Jiao Tong University, Shanghai, 200240, China*
[b] *Ocean College, Zhejiang University, Zhoushan, 316021, China*

## ARTICLE INFO

## ABSTRACT

In this paper, the self-propulsion performance of a full formed hull is optimized by the in-house hull form optimization software OPTShip-SJTU 2.1. In the field of hull form optimization, complex hull optimizations such as hull-propeller interaction optimization have not launched a full investigation. To break through this limitation, the hull-propeller interaction module is brought into the software. We conduct a hull-propeller interaction design optimization of Japan Bulk Carrier (JBC) with an actual propeller (AP) based on CFD considering ship resistance and propeller wake distortion at Fr = 0.142. Hull form deformation module is applied to change the stern shape of the JBC. The in-house CFD software naoe-FOAM-SJTU is applied to calculate the hull resistance and wake fraction. The dynamic overset grid method is used to achieve the interaction between hull and propeller and obtain the high-fidelity flow field during the optimization processing. A multi-objective genetic algorithm (NSGA-II) is applied to obtain the optimized hull forms based on the Kriging surrogate model. The influences of propeller for the flow field around stern are also studied. Results indicate: (I) OPTShip-SJTU 2.1 can optimize the coupled hydrodynamic performance in complex hull form optimization. (II) The hull resistance and wake fraction have a strong positive correlation under the deformation setting in this paper. (III) Contraction of hull line at the stern can suppress the flow separation around the stern which is benefit for reducing the pressure resistance and improving the propeller wake distortion. (IV) It is necessary to consider the interaction between propeller and hull together in hull form optimization. The interactions between the shape of stern, propeller performance, and flow field around stern are discussed preliminary, which provide several references for the subsequent research.

## 1. Introduction

Hull form optimization is one of the measures to obtain better hydrodynamic performance (resistance, seakeeping, maneuver, flow field). With the development of computational ability and the computational fluid dynamic techniques, the Simulation-Based Design (SBD) framework has been developed and applied to the hydrodynamic performance optimization of hull form (Miao and Wan, 2020a; Tahara et al., 2011; Yang et al., 2015). The optimization framework contents three main parts based on the SBD, shown as Fig. 1, described as follows:

(1) Hull form deformation module: hull form deformation tools are applied to generate a series of similar hull form samples based on the initial hull form;
(2) Hydrodynamic performance prediction module: numerical solvers are applied to predict the hydrodynamic performances of different hull form samples;
(3) Optimizer module: surrogate models and optimization algorithms are used to find the best hydrodynamic performance hull form based on surrogate model.

In the past few years, some traditional optimization studies are conducted under simplified conditions based on the SBD.

For the resistance optimization, potential flow methods are applied
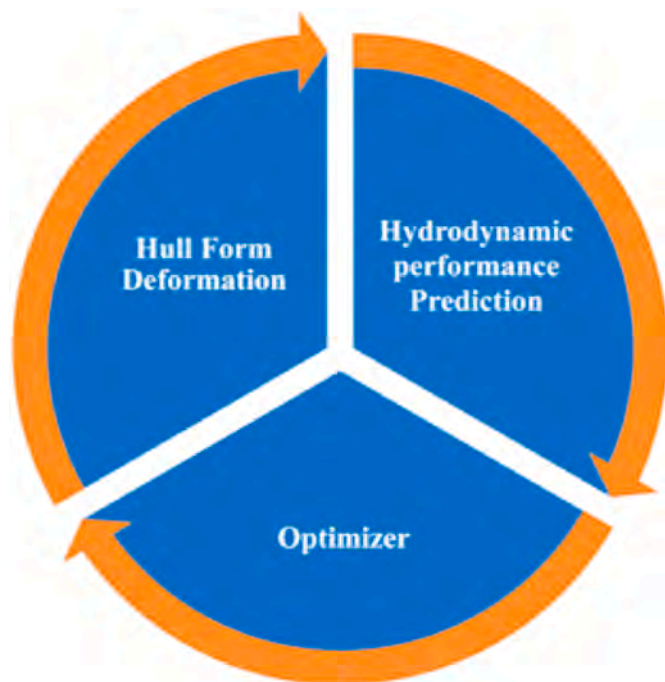
---

**Fig. 1.** The hull form optimization processing.

widely for the high-efficiency in calculating resistance. Liu et al. (2019) used the in-house hull form optimization software to minimize the total resistance of KCS in full speeds combined the Neumann-Michell theory and ITTC formula. The maximum reduction in resistance was 8.32%. Wu et al. (2016) used the Neumann-Michell theory and an extension of Bales seakeeping ranking method (Kim et al., 2010) to predict the wave-making resistance and Bales seakeeping rank factor R respectively. Nondominated Sorting Genetic Algorithm-II (NSGA-II) was applied to get the Pareto front and obtain the best hull form. Yu et al. (2017) optimized the wave-making resistance of a 66,000 DWT bulk carrier in calm water.

Compared with the potential flow theory, the viscous flow method (Computational Fluid Dynamic, CFD) achieves the visualized high-fidelity flow field and the prediction results are more accurate. Huang et al. (2015) developed a CFD-based ship hydrodynamic optimization tool to reduce the resistance and improve the seakeeping performance of hull. Zhang et al. (2018) used the viscous flow method to optimize the total resistance of two hull forms (DTMB and Wigley III) in calm water. The resistance of optimized hull form dropped by up to 5.58%. Park et al. (2015) used optimization techniques to enhance the total resistance performance of the KSUEZMAX. The total resistance was reduced by 2.4%. Further, the methods of combining potential flow and viscous flow are also used to calculate hull resistance performance (Miao and Wan, 2020b).

For propeller wake optimization, the relevant study works are relatively less compared with resistance optimization. Chen et al. (2015) used the Levenberg-Marquardt Method (LMM) and the commercial code SHIPFLOW to obtain optimal hull form based on the required wake distributions. Park et al. (2015) used the optimization tools to enhance the propulsion efficiency, and the propulsive efficiency increased by 2.0%. Ichinose and Tahara (2018) developed a proposed wake field design system to obtain an optimal hull form according to the target wake distribution. Li et al. (2019) overlaid the induced velocity field with the wake field near the front of the propeller to achieve effective wake field improvement. Feng et al. (2018) optimized an offshore aquaculture vessel to improve the resistance performance and the wake field quality. He et al. (2019a) used the adjoint method and potential method to optimize the resistance and propeller wake under self-propulsion and towing conditions. Liu et al. (2021) improved the resistance and wake performance of Japan Bulk Carrier utilizing the Liutex-based centripetal force field.

Besides bare hull hydrodynamic performance optimization mentioned above, a few study works have been carried out on the hydrodynamic performance optimization of hulls with appendages, such as hull with a propeller, rudder, and other appendages. Compared with a bare hull, the hull with appendages is closer to the real sailing condition of ship. Thus, the studies of hull form optimization with appendages are receiving more and more attention from scholars. Sun and Zhao (2019) studied three types of bow appendages (triangle fins, rectangular foil, and semi-submerged body) that impact the total resistance, and the best Fr number corresponding to the lowest resistance for each bow appendage was found. Liu et al. (2020) proposed a new type of bow appendage and investigate the influence of appendage installation position on resistance. Finally, the new type of bow appendage can achieve resistance reduction by 8%. He et al. (2019b) utilized actuator disk theory to mimic the impact of propellers and optimized the hull resistance and propeller wake. As the computational ability improvement, some complex hull form optimization with appendages is conducted. Guo et al. (2020) studied the multi-objective optimization of a waterjet-propelled trimaran. It achieved optimization of the actual propeller and trimaran hull interaction in hull form optimization based on the CFD.

We can realize many optimization works of resistance and wake have been done using different methods. Hull form optimization is the optimization of the whole hull system and must consider the influence of other appendages(Wang et al., 2019), and the changes in hull form can also affect the hydrodynamic performance of the appendages. Hull-appendages interaction optimization researches have not been studied fully yet. It is necessary to consider the appendages during the optimization process and study interaction optimization between the main hull forms and appendages.

The purpose of our work is to take advantage of the in-house hull form optimization software OPTShip-SJTU 2.1 to optimize a hull appended with an actual propeller under model scale. The Japan Bulk
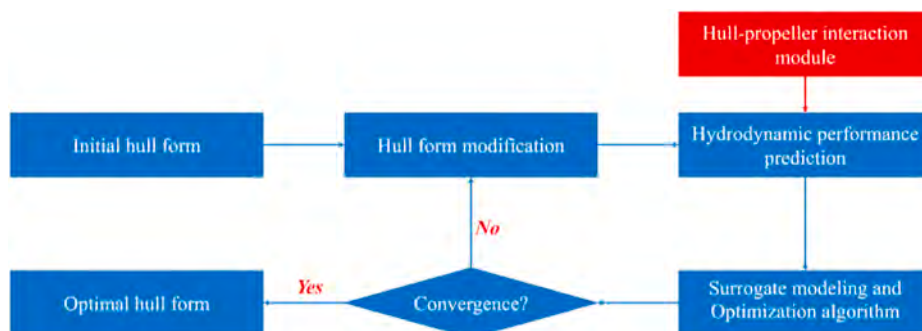


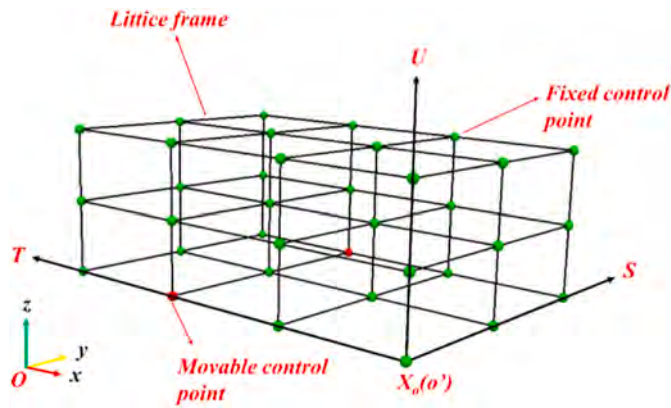**Fig. 2.** The framework of OPTShip-SJTU 2.1.

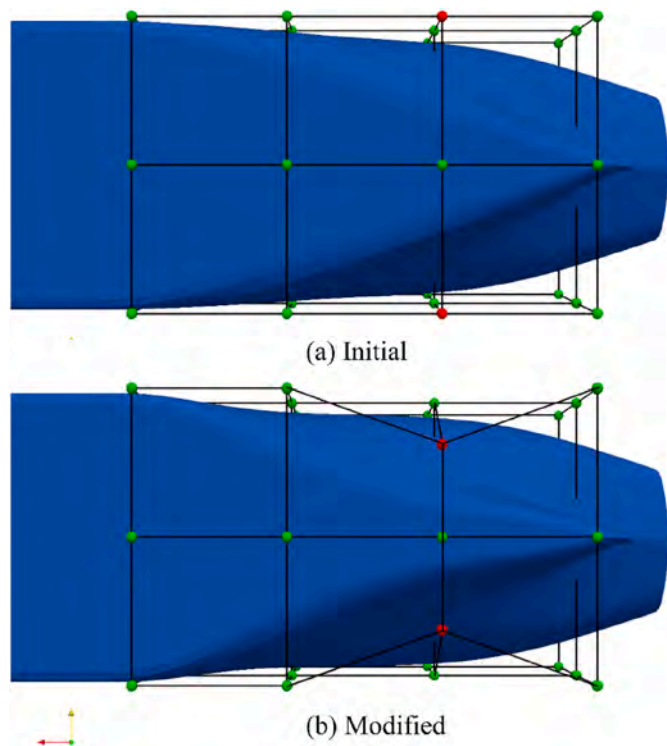**Fig. 3.** The local coordinate system of the FFD method.



**Fig. 4.** The hull form deformation based on the FFD.

Carrier (JBC) (Hirata et al., 2021) is selected as the baseline hull geometry at the model scale and the present study is for model scale performance. Firstly, the Free-Form Deformation method (FFD) is applied to modify the initial hull form and create a series of similar hull forms utilizing the Optimized Latin Hypercube Design (OLHD). Secondly, the high-fidelity flow fields of different hull forms are predicted by the in-house viscous solver naoe-FOAM-SJTU considering hull-propeller interaction simultaneously. Thirdly, the multi-objective Kriging surrogate model is established to describe the relationship between objectives and parameters. A series of optimized hull forms obtained from the Pareto Front can be gotten by NSGA-II.

The remaining part of the paper proceeds as follows. In section 2, we introduce the optimization framework of the OPTShip-SJTU 2.1, and the methods used in this paper are described (hull form deformation method, hydrodynamic performance calculation method, and optimization algorithm). In section 3, the resistance and propeller wake distortion optimizations of JBC are conducted utilizing the OPTShip-SJTU 2.1. The optimization results and discussions are presented in

section 4. The summaries are placed in section 5.

## 2. Methods

### 2.1. In-house optimization software OPTShip-SJTU 2.1

In our study, the in-house hull form optimization software OPTShip-SJTU 2.1 is applied. The framework of this software is shown in Fig. 2 Comparing with the older versions of the software, the overset grid technique has been incorporated to achieve the coupled motion between the hull and its appendages (hull-propeller interaction module).

It includes three modules:

(1) the hull form deformation module;
(2) hydrodynamic performance prediction module;
(3) optimizer: it includes surrogate model and optimization algorithm;

The relevant theories used in our study work are introduced briefly in the following content.

### 2.2. Hull form deformation methods

The hull form modification module is used to change the shape of the initial hull to create a series of different hull forms based on the initial hull. The hull form deformation methods have Free-From Deformation (Liu C. et al., 2020), Shifting Method(Kim et al., 2010), and Radial Basis Function Method (Liu et al., 2019) in the hull form deformation module. In this paper, the Free-Form Deformation (FFD) is applied to modify the stern shape of JBC. FFD has been widely used in industry fields (Campana et al., 2009; Chen et al., 2015), which was firstly proposed by Sederberg and Parry (1986). The basic idea is embedding an object within a lattice which is trapezoidal or other topology structures and the object is modified as the lattice is modified.

A local coordinate system $O'$-$STU$ is established according to the lattice, like Fig. 3.

Where $O'$ is the local coordinate origin, $S$, $T$, and $U$ is the three-axis under the local coordinate system. Assumption, point $X$ under the Cartesian coordinate system point can be described as ($s$, $t$, $u$) under the local coordinate system $o'$-$STU$, then

$$\mathbf{X} = \mathbf{X_0} + s\mathbf{S} + t\mathbf{T} + u\mathbf{U} \qquad (1)$$

$X_0$ is the origin point under the local coordinate system, $s$, $t$, $u$ can describe, as shown below:

$$s = \frac{\mathbf{T} \times \mathbf{U} \cdot (\mathbf{X} - \mathbf{X_0})}{\mathbf{T} \times \mathbf{U} \cdot \mathbf{S}} \qquad (2)$$

$$t = \frac{\mathbf{S} \times \mathbf{U} \cdot (\mathbf{X} - \mathbf{X_0})}{\mathbf{S} \times \mathbf{U} \cdot \mathbf{T}} \qquad (3)$$

$$u = \frac{\mathbf{S} \times \mathbf{T} \cdot (\mathbf{X} - \mathbf{X_0})}{\mathbf{S} \times \mathbf{T} \cdot \mathbf{U}} \qquad (4)$$

The value of $s$, $t$, and $u$ are in the range [0,1].

The lattice is divided into small regions equally along with the $S$, $T$, and $U$ axis. Assumption, the lattice is divided into $l$, $m$, and $n$ along with the $S$, $T$, and $U$ directions equally. Control points are defined as lattice nodes, and the control point $Q_{ijk}$, described as

$$\mathbf{Q}_{i,j,k} = \mathbf{X_0} + \frac{i}{l}\mathbf{S} + \frac{j}{m}\mathbf{T} + \frac{k}{n}\mathbf{U} \qquad (5)$$

Within $i$ = 0, 1,2, ......$l$; $j$ = 0, 1,2, ......$m$; $k$ = 0, 1,2, ......$n$;

Thus, any point located in the lattice can be described as Eq. (6) under the Cartesian coordinate system:

$$\mathbf{X}(s,t,u) = \sum_{i=0}^{l} \sum_{j=0}^{m} \sum_{k=0}^{n} B_{i,j}(s)B_{j,m}(t)B_{k,n}(u)\mathbf{Q}_{i,j,k} \tag{6}$$

With $B$ is the Bernstein polynomial basis function, which is defined as:

$$B_{i,n}(u) = \frac{n!}{i!(n-i)!}u^i(1-u)^{n-i} \tag{7}$$

After the relationship between the ship surface points and the lattice control points is established, we can modify the hull form by moving the relative control points. After moving, the new control point is $\mathbf{Q}'_{ijk}$, X will change into $\mathbf{X}_{ffd}$:

$$\mathbf{X}_{ffd} = \sum_{i=0}^{l} \sum_{j=0}^{m} \sum_{k=0}^{n} B_{i,j}(s)B_{j,m}(t)B_{k,n}(u)\mathbf{Q}'_{i,j,k} \tag{8}$$

The new hull forms can be obtained by changing the number, direction, and magnitude of the movable control points. A lattice is applied to surround the stern of JBC, and the deformation effect of the FFD method is shown in Fig. 4.

### 2.3. Hydrodynamic performance prediction methods

After obtaining a series of hull form samples, firstly, we use the benchmark case to verify the precision of the solver and compare the calculated results with the experimental results (experimental fluid dynamic, EFD). The aim is to ensure the accuracy of calculated results by this solver. Secondly, the verified solver is used to calculate the hydrodynamic performance of other hull form samples. In this paper, the in-house viscous solver naoe-FOAM-SJTU is used to calculate the resistance and wake fraction(Ren et al., 2020; Wang et al., 2018). It is developed based on the open-source CFD software OpenFOAM, we only give a brief introduction. More information can refer to Wang et al. (2016) and Shen et al. (2015).

The flow governing equations are unsteady Reynolds-Averaged Navier-Stokes (URANS) equations, which are presented as mass conservation equation and momentum conservation equation, as follow:

$$\nabla \cdot \mathbf{U} = 0 \tag{9}$$

$$\frac{\partial \rho \mathbf{U}}{\partial t} + \nabla \cdot \left(\rho(\mathbf{U}-\mathbf{U_g})\mathbf{U}\right) = -\nabla p_d - \mathbf{g}\cdot\mathbf{x}\nabla\rho + \nabla\cdot\left(\mu_{eff}\nabla\mathbf{U}\right) + (\nabla\mathbf{U})\cdot\nabla\mu_{eff}$$
$$+ \mathbf{f}_\sigma \tag{10}$$

Within $\mathbf{U}$ is the velocity of the flow field, $\mathbf{U_g}$ is the velocity of grid nodes. $p_d = p-\rho\mathbf{g}\cdot\mathbf{x}$ is the dynamical pressure, $p$ is the total pressure. $\rho$ is the flow density, $\mathbf{g}$ is the gravity acceleration. $\mu_{\text{eff}} = \rho(\nu + \nu_t)$ is the effective dynamical viscosity, in which $\nu$ and $\nu_t$ are kinematic viscosity and kinematic eddy viscosity, respectively. $\nu_t$ is obtained from the turbulence model which is a blended $k-\omega/k-\varepsilon$ shear stress transport (SST) model (Menter et al., 2003). $\mathbf{f}_\sigma$ is the source term for surface tension. The velocity gradient near the wall is resolved by the wall function.

The Volume of Fluid (VOF) approach with bounded compression technique is used to capture the free face, the transport equation is presented as follow:

$$\frac{\partial \alpha}{\partial t} + \nabla \cdot \left[(\mathbf{U}-\mathbf{U_g})\alpha\right] + \nabla \cdot [\mathbf{U_r}(1-\alpha)\alpha] = 0 \tag{11}$$

where $\alpha$ is the volume of fraction, $0 < \alpha < 1$ represents the interface between two-phase fluid, $\alpha = 1$ represents water, and $\alpha = 0$ represents air. $\mathbf{U_r}$ is the velocity field used to compress the interface which only takes effect on the free surface. The $(1-\alpha)\alpha$ term guarantees boundedness and the "$\nabla\cdot$" guarantees conservation (Wang J. et al., 2019).

The velocity field and pressure field are solved by the merged PISO-SIMPLE (PIMPLE) algorithm in naoe-FOAM-SJTU. The pressure implicit

splitting operator (PISO) algorithm and the semi-implicit method for pressure linked equations (SIMPLE) are provided by OpenFOAM. The numerical schemes provided by OpenFOAM are also used to discretize the partial differential equations. A second-order central TVD limited linear scheme is used to discretize the convection terms. The diffusion terms are solved by a second-order central difference scheme. An implicit Euler scheme is used to deal with temporal discretization.

The dynamic overset grid method is applied in the in-house solver naoe-FOAM-SJTU, which can remove the restrictions of the mesh topology among different objects and allow grids to move independently within the computational domain. It can be used to handle large amplitude motion in the field of ship and ocean engineering (Liu C. et al., 2020; Wang et al., 2018), and the overset grid technique allows the ship and the propeller to move simultaneously in 6 DOF. There are two coordinate systems in solving the 6 DOF equation, one is the earth-fixed system and the other is the ship-fixed system (non-inertial system). The ship-fixed system is fixed to the ship and can translate or rotate along with the ship motions. For more information about the 6 DOF motion solver with the overset grid in naoe-FOAM-SJTU, it is introduced in this reference (Shen et al., 2015). In this paper, this technique can achieve the relative motion between the main hull and the propeller. The type of grid cell is divided into 5 for the overset grid method, active cells, fringe/interpolated cells, hole cells, donor cells, and orphan cells.

In the code solver, the information of grid cells is stored in the domain connectivity information file (DCI). The suggar++ (Noack et al., 2009) is utilized to achieve the information exchange during the several grid types. One of the out-standings of the solver is combing the Open-FOAM and the suggar++ to achieve the complex calculation in the field of ship and ocean engineering. For more information, please refer to Wang et al. (2016) and Shen et al. (2015).

### 2.4. Optimizer

The optimizer includes two parts: the surrogate model and the optimization algorithm. For searching the best hydrodynamic performance hull form, the functional relationship between the objective functions (such as resistance, wake fraction, and so on) and the hull form deformation parameters should be established by the surrogate model. The hull form deformation parameters are obtained by the design of experiments (DOE). The design of experiments is a strategy for choosing samples in the design space. Many DOE methods have been applied in hull form optimization, such as Latin hypercube sampling (LHS), Optimized Latin Hypercube sampling (OLHS), factorial design, and so on. Optimized Latin Hypercube Sampling (OLHS) is widely used to select samples as a design-of-experiment technique (Liu et al., 2011). The OLHS is utilized to obtain different deformation parameters from the design space in this paper. A series of hull form samples are gotten by the hull form deformation module according to the hull form deformation parameters. The naoe-FOAM-SJTU is utilized to predict the hydrodynamic performance of different hull forms based on CFD.

After getting the hydrodynamic performance of different hull forms, the surrogate model is applied to establish the relationship between the hydrodynamic performance and the hull form deformation parameters. The surrogate models have the Kriging model(Lin et al., 2018), Response surface methodology (RSM)(Kim et al., 2011), the neural network(Z. Liu et al., 2020), and so on. The Kriging surrogate model is used to find the functional relationship between the objective functions and the hull form deformation parameters. The Kriging model can be described as a stochastic process approach:

$$y(\mathbf{x}^{(i)}) = \mu + \varepsilon(\mathbf{x}^{(i)}) \quad (i = 1, \cdots, n) \tag{12}$$

$\mu$ is the average value of stochastic processes. $\varepsilon(\mathbf{x}^{(i)})$ satisfy normally distributed ($0~\sigma^2$), and non-zero covariance, which is given by follows:
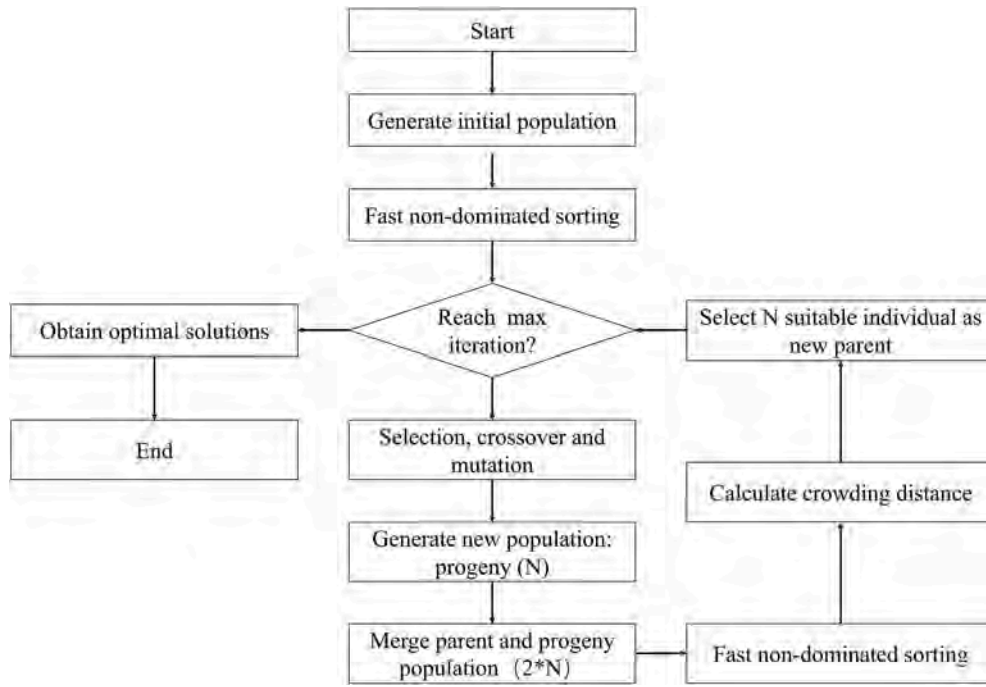
**Fig. 5.** Flow chart of NSGA-II

$$\mathrm{Cov}\big[\varepsilon\big(\mathbf{x}^{(i)}\big),\varepsilon\big(\mathbf{x}^{(j)}\big)\big]=\sigma^2\mathbf{R}\big(\big[\mathrm{Corr}\big[\varepsilon\big(\mathbf{x}^{(i)}\big),\varepsilon\big(\mathbf{x}^{(j)}\big)\big]\big]\big) \tag{13}$$

$$\mathrm{Corr}\big[\varepsilon\big(\mathbf{x}^{(i)}\big),\varepsilon\big(\mathbf{x}^{(j)}\big)\big]=\exp\big[-d\big(\mathbf{x}^{(i)},\mathbf{x}^{(j)}\big)\big] \tag{14}$$

$$d\big(\mathbf{x}^{(i)},\mathbf{x}^{(j)}\big)=\sum_{h=1}^{k}\theta_h\big|x_h^{(i)}-x_h^{(j)}\big|^{p_h},\quad \theta_h\geq0,\quad p_h\in[1,2] \tag{15}$$

*R* is the $n\times n$ matrix. its (i,j) element is $Corr[\varepsilon(x^{(i)}),\varepsilon(x^{(j)})]$. Eq. (14) denotes gaussian correlation function.

The estimate values of $\mu$ and $\sigma^2$ can be obtained combining the correlation parameters (the $\theta_h$ and $p_h$). $\mu,\sigma^2,\theta_1,...,\theta_k,p_1,...,p_k$ are gotten by maximizing the likelihood of the samples. $\mathbf{y}=(y^{(1)},...,x^{(n)})'$ are sampled data points. The likelihood function is:

$$\frac{1}{(2\pi)^{n/2}(\sigma^2)^{n/2}|\mathbf{R}|^{\frac{1}{2}}}\exp\left[-\frac{(\mathbf{y}-\mathbf{1}\mu)'\mathbf{R}^{-1}(\mathbf{y}-\mathbf{1}\mu)}{2\sigma^2}\right] \tag{16}$$

Given the correlation parameters $\theta_h$ and $p_h$, ($h=1,...,k$), the estimated $\mu$ and $\sigma^2$ can be gotten by maximizing the likelihood function. The $\mu$ and $\sigma^2$ can be expressed as:

$$\widehat{\mu}=\frac{\mathbf{1R}^{-1}\mathbf{y}}{\mathbf{1}'\mathbf{R}^{-1}\mathbf{1}} \tag{17}$$

$$\widehat{\sigma}^2=\frac{(\mathbf{y}-\mathbf{1}\widehat{\mu})\mathbf{R}^{-1}(\mathbf{y}-\mathbf{1}\widehat{\mu})}{n} \tag{18}$$

For a new variable $x^*$, defining $r$ as correlation vector between the new variable $x^*$ and sample data. $r$ is expressed as:

$$r_i(\mathbf{x}^*)=\mathrm{Corr}\big[\varepsilon\big(\mathbf{x}^*\big),\varepsilon\big(\mathbf{x}^{(i)}\big)\big] \tag{18}$$

Utilizing Eq. (14) and Eq. (15), the predicted value at the new position $x^*$:

$$\widehat{y}(\mathbf{x}^*)=\widehat{\mu}+\mathbf{r}'\mathbf{R}^{-1}(\mathbf{y}-I\widehat{\mu}) \tag{19}$$

Based on the surrogate model, the optimization algorithm is used to search the optimized hydrodynamic performance hull and the corresponding optimized hull form deformation parameters. The optimized

hull form needs to be calculated by the solver to verify the theoretical optimized results. The multi-objective optimization algorithm is utilized in many fields of science. A multi-objective optimization problem can be described as:

$$\begin{aligned}minimize\quad &(f_1(\mathbf{x}),f_2(\mathbf{x}),...,f_k(\mathbf{x})),\quad k=1,\cdots,n\\ subject\,to\quad &g_i(\mathbf{x})\leq0,\quad i=1,\cdots,p\\ &h_j(\mathbf{x})=0,\quad j=1,\cdots,q\end{aligned} \tag{20}$$

where $f_k$ is the *k* objective function and the $\mathbf{x}=(x_1,...,x_m)$ are the design parameters. $g_i(\mathbf{x})\leq0$ is the inequality constraint and $h_j(\mathbf{x})=0$ is the equality constraint. In this paper, Non-dominated Sorting Genetic Algorithm II (NSGA) (Deb et al., 2002) is used to solve the multi-objective optimization problem and obtain the Pareto Front. There are three improvements.

(1) Fast non-dominated sorting is applied to speed up algorithm convergence.

(2) Crowding distance is defined to make the distribution of the Pareto Front more evenly. The crowding distance of the *i* individual $D_i$ is defined as:

$$D_i=\sum_{j=1}^{n}\big[\big(f_{i+1,j}-f_{i-1,j}\big)\big/\big(f_{\max,j}-f_{\min,j}\big)\big] \tag{21}$$

where $f_{i+1,j}$ is the *j* objective value of the $i+1$ individual. $f_{i-1,j}$ is the *j* objective value of the $i-1$ individual. $f_{max,j}$ denote the maximum value of the *j* objective. $f_{min,j}$ denote the minimum value of the *j* objective.

(3) The elite strategy is used to expand sampling space and accelerate population evolution.

The process of NSGA-II is shown in Fig. 5. The detailed information about NSGA-II can be gotten for reference(Zhu and Ma, 2019).

**Table 1**
The model principle parameters of the main hull.

| Parameters | Value |
| --- | --- |
| $L_{pp}$(m) | 7.000 |
| $L_{wl}$(m) | 7.125 |
| T(m) | 0.413 |
| S(m$^2$) | 12.223 |
| $\bigtriangledown$(m$^3$) | 2.787 |

**Table 2**
The model principle parameters of the propeller.

| Parameters | | Value |
| --- | --- | --- |
| Diameter(mm) | | 203.000 |
| Boss ratio | | 0.180 |
| Pitch(constant) | | 152.250 |
| Pitch ratio | | 0.750 |
| Expanded area ratio | | 0.500 |
| Blade thickness ratio | | 0.050 |
| Angle of rake | | 5.000 |
| Position of Propeller | $x/L_{pp}$ | 0.9857 |
| | $-z/L_{pp}$ | $-0.0404$ |

## 3. Verification

### 3.1. Geometry model

In our study, the JBC (Japan Bulk Carrier) is selected as the base geometry and the present study is for model scale performance. Towing tank experiments of JBC are conducted at NMRI, SRC, and Osaka University (Hino et al., 2020), which include resistance tests, self-propulsion tests, and PIV measurements of stern flow fields. Benefitting from the experiment data, we can compare numerical simulation results with physical experiment results to verify the accuracy of numerical simulation results. To get closer to the real sailing state, the actual propeller is considered during numerical simulation. The principle model parameters of JBC and propeller are shown in Table 1 and Table 2. The model is shown in Fig. 6. The speed of the hull is 1.179 m/s (Fr = 0.142). The free surface affects the hull hydrodynamic performance, which further affects the propeller hydrodynamic performance. The percentage of wave-making resistance is small, but it still affects the hull resistance. Therefore, a two-phase solver must be more reliable than a single-phase solver. The two-phase viscous solver naoe-FOAM-SJTU is applied to consider the free surface effects.

The optimization process of JBC includes three parts:

(1) Modifying the shape of the stern.
(2) The numerical simulation results of JBC are compared with the experimental results to verify the accuracy of the solver naoe-FOAM-SJTU, and then the hydrodynamic performances of different hull forms are calculated to obtain the hydrodynamic performance database (resistance and wake fraction).
(3) a reliable Kriging model is applied to establish a mapping relationship between the deformation parameters and hydrodynamic performances. The NSGA-II is used to search the optimized hull forms. An optimized point is selected from Pareto Front to verify the optimization effect. According to the optimized deformation parameters, the optimized hull form can be obtained utilizing the hull form deformation module. Then, the naoe-FOAM-SJTU is used to calculate the hydrodynamic performance of the optimized hull form. Finally, the differences between the initial hull form and the optimized hull form are summarized.



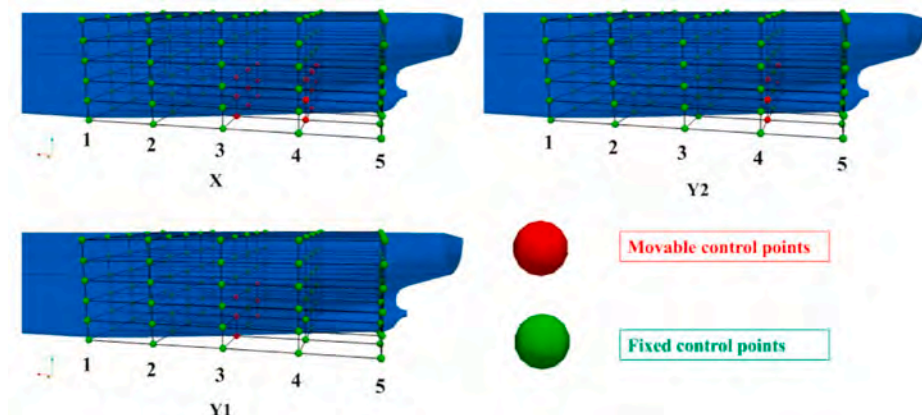**Fig. 6.** The model of hull and propeller.



**Fig. 7.** The lattice zone and control points distribution.

**Table 3**
The deformation parameter design spaces (when the $L_{pp} = 1$ m).

| Parameter | Range (m) |
|---|---|
| $X$ | [-0.02,0.02] |
| $Y1$ | [-0.05,0.05] |
| $Y2$ | [-0.03,0.03] |

### 3.2. Design space construction and deformation setup

Considering the low wave-making resistance, we focus on modifying the stern shape to optimize the viscous resistance and the propeller wake distortion. Three deformation parameters are selected to control the shape of the stern, $X$, $Y1$, and $Y2$. The $X$ controls the deformation of the stern along the x-direction at the third and fourth plane of the lattice. The $Y1$ controls the deformation of the stern along the y-direction at the third plane of the lattice. The $Y2$ controls the deformation of the stern along the y-direction at the fourth plane of the lattice. Fig. 7 shows the lattice zone at the stern. Considering the volume of displacement, hull shape symmetric, the surface curvature, and so on, the design space of the deformation parameters is set shown in Table 3. According to the design space, the different hull deformation parameters can be gotten by the Optimized Latin Hypercube Sampling Method (OLHS) (Feng et al., 2018; Ferrari et al., 2019). The sampling points distribution in design space is shown in Fig. 8. Finally, 30 sampling points are obtained through the OLHS method and 30 hull forms are also created by the FFD method based on the deformation parameters.

### 3.3. CFD configuration

One of our works is the self-propulsion computation of JBC ship

model. According to the experiment fluid dynamic setting, the speed is set to 1.179 m/s, corresponding to Fr = 0.142. The OpenFOAM mesh tool *snappyHexMesh* is used to generate the fully unstructured hexahedral mesh in this paper. To achieve the coupled motion between the hull and propeller, there are three parts in the computational domain: background grid, hull grid, and propeller grid. The dynamic overset grid method is applied to achieve the information exchange between three grids at the grid overset region. The total grid num is 7.3 million, shown in Table 4. Fig. 9 and Fig. 10 show the computational domain and overset grid arrangement.

Pitching motion and heaving motion of the hull are released. For accelerating the numerical simulation, the *MapField* tool is applied during the numerical simulation, which is a pre-processing flow field mapping tool in OpenFOAM. For capturing the wave-making at the free surface, the grid refinement at the free surface is adopted. For capturing the flow around the hull, the number of boundaries is set as 8. For the propeller mesh, the boundary layer is set as 5. The average y+ is around 30 for the bodies. The boundary condition of the inlet is zero gradients and zero velocity, which is identical to farfield boundaries. A pressure outlet boundary condition is applied for the outlet boundary.

**Table 4**
The grid number allocation for the CFD calculation.

| Grid | Number (million) |
|---|---|
| Background | 1.41 |
| Hull | 3.08 |
| Propeller | 2.88 |



(a) The distribution of Y1 and Y2

(b) The distribution of Y1 and X

(c) The distribution of Y2 and X

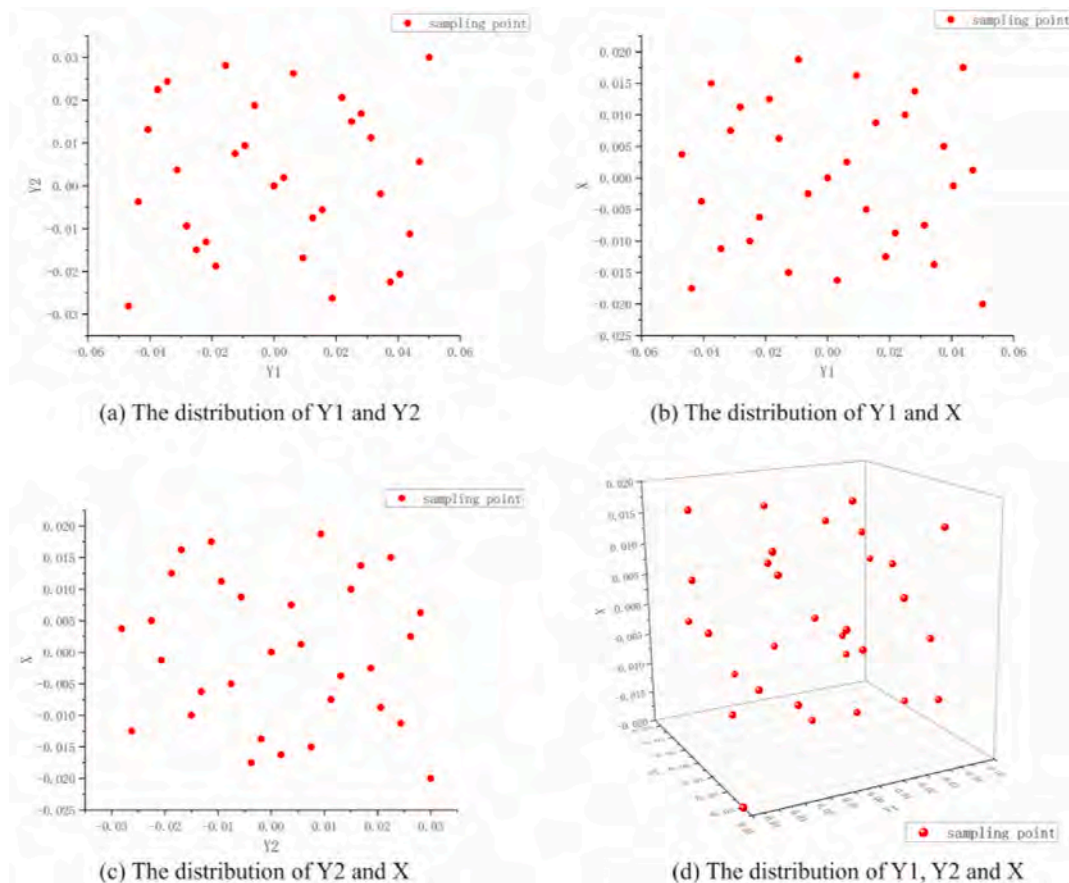(d) The distribution of Y1, Y2 and X

**Fig. 8.** The sampling points distribution in design spaces.
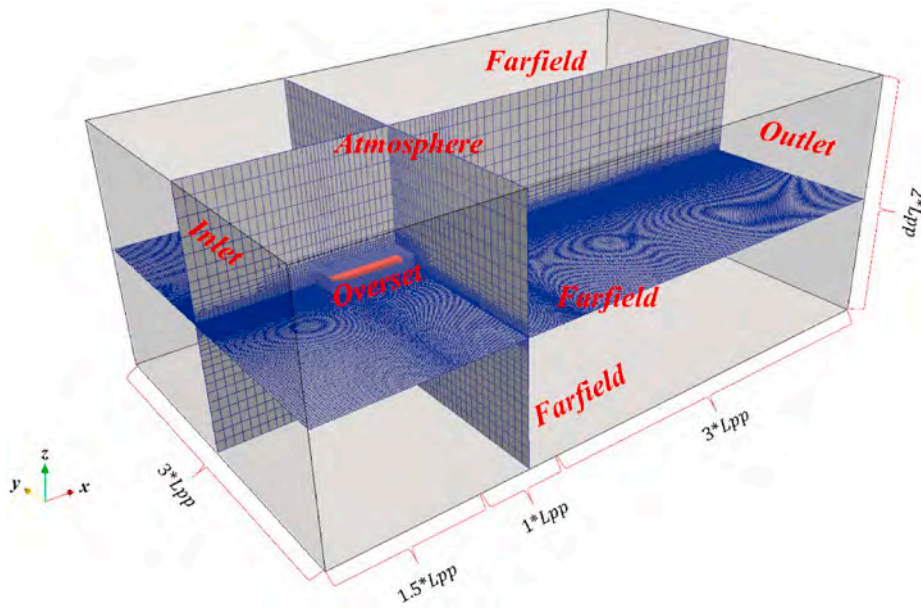
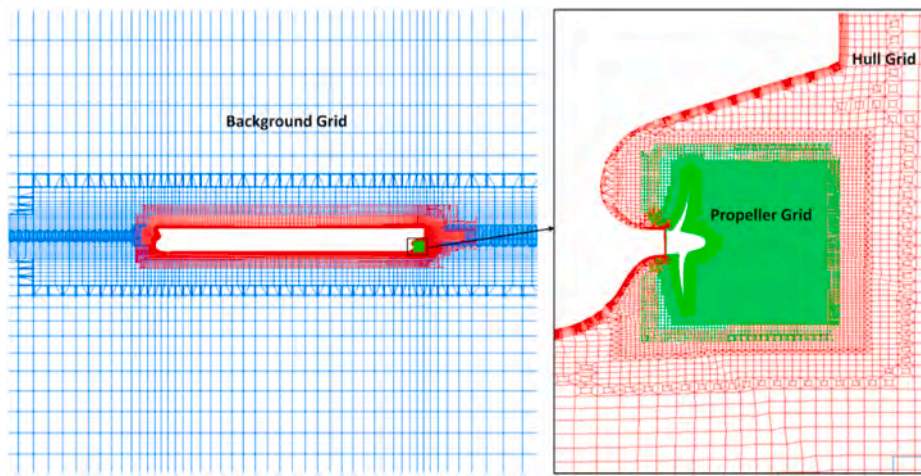**Fig. 9.** The CFD domain.



**Fig. 10.** The overset grid distribution (background grid, hull grid, and propeller grid).

**Table 5**

Comparison between the experimental fluid dynamic (EFD) and the computational fluid dynamic (CFD).

| parameters | EFD | CFD | Relative Error |
|---|---|---|---|
| $C_t$ | $4.811*10^{-3}$ | $4.63*10^{-3}$, | 3.81% |
| $n$ | 7.8 rps | 7.75 rps | 0.65% |

### 3.4. CFD validation

In this part, the hydrodynamic performance of the initial JBC hull form is calculated to assess the accuracy of naoe-FOAM-SJTU. The grid convergence verification and uncertainty estimation are also conducted. The numerical simulation results (total resistance coefficient $C_t$, propeller rotation speed $n$) are compared with the experimental data measured by National Maritime Research Institute (NMRI). The grid number allocation is shown in Table 4. The simulated $C_t = 4.63*10^{-3}$, which is 3.76% lower than the experimental value $4.811*10^{-3}$, the propeller rotation speed simulated value is 7.75 rps, which is lower 0.64% than the experimental value 7.8 rps, shown in Table 5. The results

demonstrate the prediction precision of naoe-FOAM-SJTU satisfies the requirement. The error keeps less than 5%. Fig. 11 and Fig. 12 are the stream-wise velocity contour comparisons between the numerical calculation result and experimental result. The contour values of numerical calculation agree well with the experiment value from Figs. 11 and 12, therefore, the calculated value of wake fraction obtained from Eq. (28) which is used to quantify propeller wake distortion satisfies the requirement of calculation accuracy. According to the validation results, the calculated wake faction of the initial hull form is 0.350. The wake fraction value is close to the actual value which can refer to the reference (Kinaci et al., 2020). Fig. 12 shows the stream-wise velocity contour at the plane corresponding to $x/L_{pp} = 1$.

Considering the uncertainties of numerical simulation, the grid convergence analysis is conducted. The grid uncertainty study is described in Wang J. et al. (2019) before. The formula of grid convergence ($R_G$) is defined as fellow:

$$R_G = \frac{S_2 - S_1}{S_3 - S_2} \tag{22}$$

where $S_1, S_2, S_3$, correspond to fine gird, medium grid, and coarse grid.
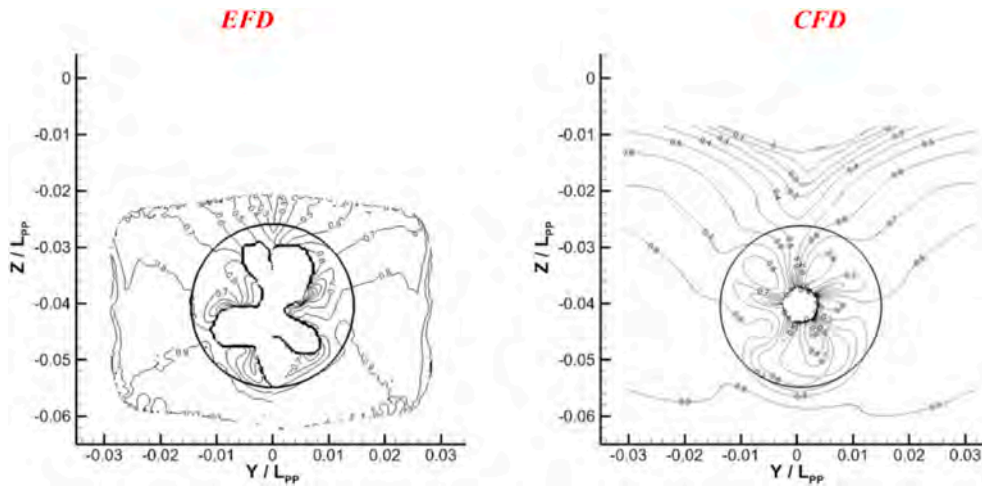
**Fig. 11.** The comparison between the experimental values and the calculated values at *x/Lpp = 0.9843*, the blade angle is 48 [deg].
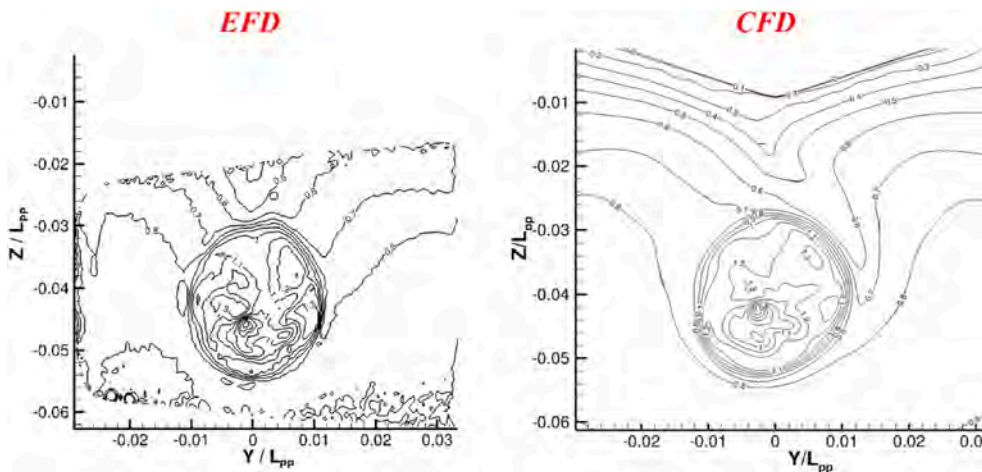


**Fig. 12.** The comparison between the experimental values and the calculated values at *x/L_{pp} = 1.00*, the blade angle is 24 [deg].

**Table 6**
The grid convergence verification.

| Mesh | $C_t$ | $K_T$ |
|---|---|---|
| Coarse | $4.60*10^{-3}$ | 0.209 |
| Medium | $4.63*10^{-3}$ | 0.207 |
| Fine | $4.64*10^{-3}$ | 0.208 |
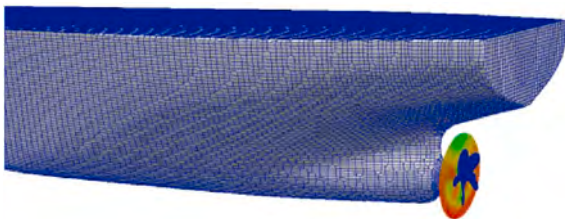


**Fig. 13.** The location of sampling plane, $x/L_{pp} = 0.9843$.



**Fig. 14.** The Pareto Front of objective function 1 (*w*) and objective function 2 ($C_t$).

$R_G < 0$ represents oscillatory convergence, $0< R_G < 1$ represents monotonic convergence, $R_G > 1$ represents divergence. Because the wake fraction obtained from Eq. (28) isn't measured in the experiment, the resis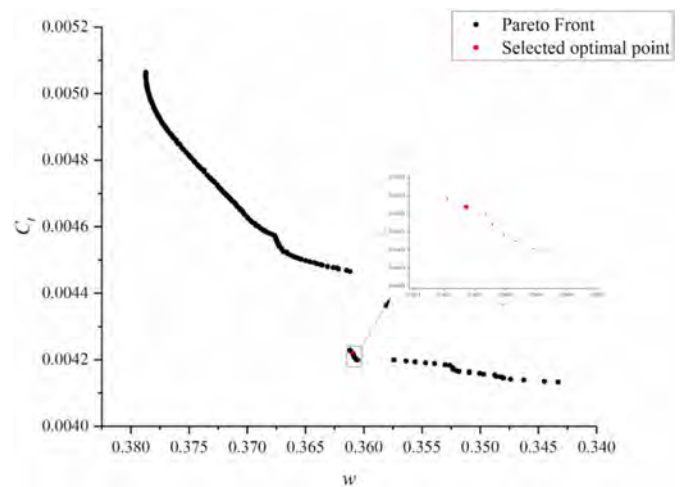tance coefficient $C_t$ and the propeller thrust factor $K_T$ are selected to conduct the grid convergence and grid uncertainty estimation, refinement ratio $r = \sqrt{2}$. The results show in Table 6.

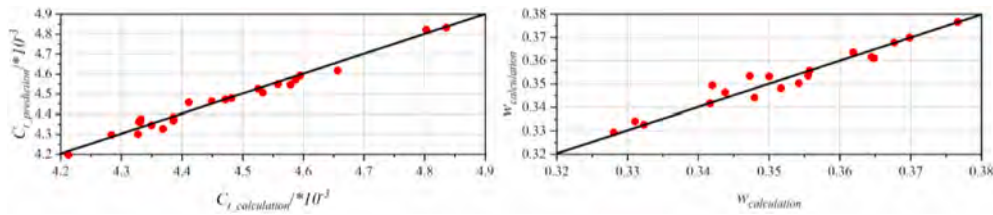The results calculated by three meshes are similar, the error

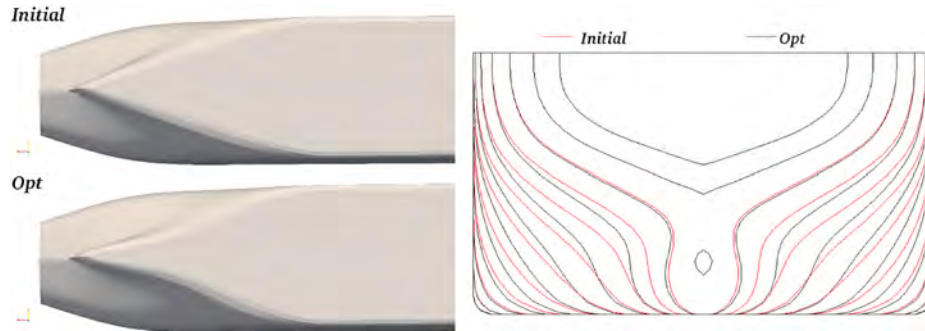**Fig. 15.** Cross validations of the surrogate models about two objective functions.



**Fig. 16.** The latter half of the hull form comparison between the initial hull form and the optimized hull form.

**Table 7**
The optimization results.

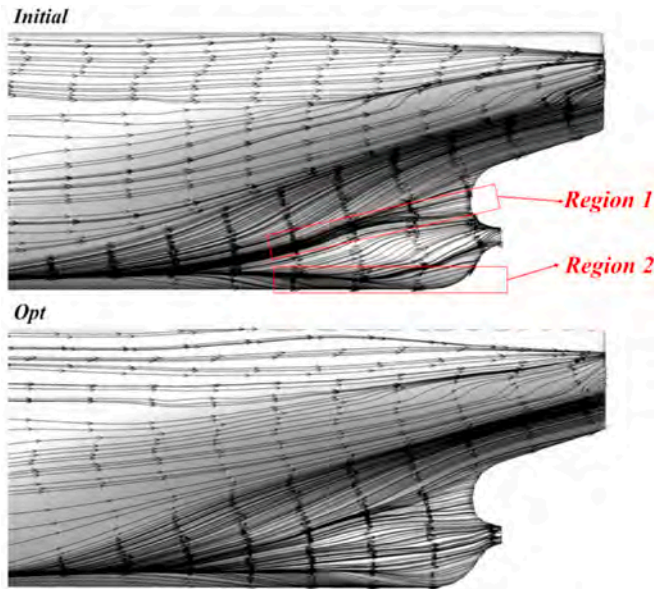|  | $C_t$ | w |
|---|---|---|
| Initial Hull | $4.630*10^{-3}$ | 0.350 |
| Optimized Hull | $4.191*10^{-3}$ | 0.361 |
| Optimized amplitude | 9.48% | 3.14% |



**Fig. 17.** The comparison of streamlines at the stern between the initial hull and the optimized hull.

compared with the experimental value is less than 5%. At the same time, the $R_G$ of $C_t$ is 0.33, corresponding to the monotonic convergence. The uncertainty $U_G$ of $C_t$ is estimated by Richardson Extrapolation method (Roache, 1998). The order of discretization is defined as follows:
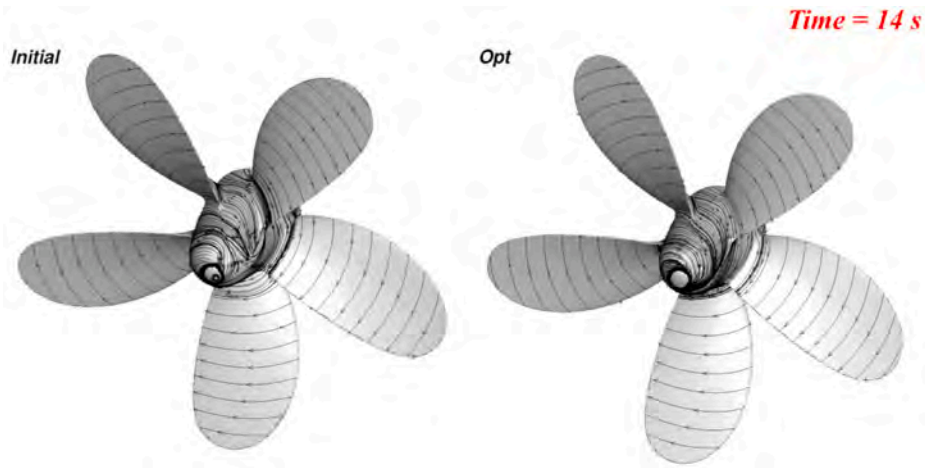
$$P = \frac{\ln(1/R_G)}{\ln(r)} \tag{23}$$

The grid convergence index (GCI) is defined as follows:

$$GCI_{ij} = Fs \frac{|e_{ij}|}{r^p - 1} \tag{24}$$

where $F_s$ is the safety factor, $F_s = 1.25$, $e_{ij}$ is the error between the $S_i$ and $S_j$. GCI denotes the error using different grids. The $GCI_{12}$ of $C_t$ is 0.132%, and $GCI_{23}$ of $C_t$ is 0.399%.

The $R_G$ of $K_T$ is $-0.5$, corresponding to the oscillatory convergence. For the oscillatory convergence, we use the average to estimate the grid uncertainty(Stern et al., 2006), as Eq. (25), the $U_G$ of $K_T$ is 0.610%.

$$U_G = \frac{1}{2}(S_{max} - S_{min}) \tag{25}$$

For accelerating the simulation and guarantying calculated precision, we select the medium grid to calculate the hydrodynamic performance of different hull forms.

### 3.5. Optimization problem

Benefitting from the high-performance computational source, four months are taken to obtain high-fidelity flow information about different hull forms. Based on the flow information about different hull forms, the surrogate model can be established. The optimization objectives should be defined first. Considering the practical application, designing a lower resistance and higher propeller hydrodynamic performance hull form is necessary. Thus, the resistance and propeller wake distortion are selected as the optimization objectives. The resistance coefficient is defined as Eq. (26) and Eq. (27).

$$R_t = R_{t(sp)} + SFC \tag{26}$$

$$C_t = \frac{R_t}{0.5\rho V^2 S} \tag{27}$$

The $R_t$ is the total resistance of the hull, the $R_{t(sp)}$ is the propeller thrust; the $SFC$ is the subjoin frictional resistance correction (SFC), $SFC = 18.2\ N$; $\rho$ is the density of water, $V$ is the velocity of the hull (1.179 m/

Time = 14 s

Initial    Opt

**Fig. 18.** propeller surface flow comparison.

Initial

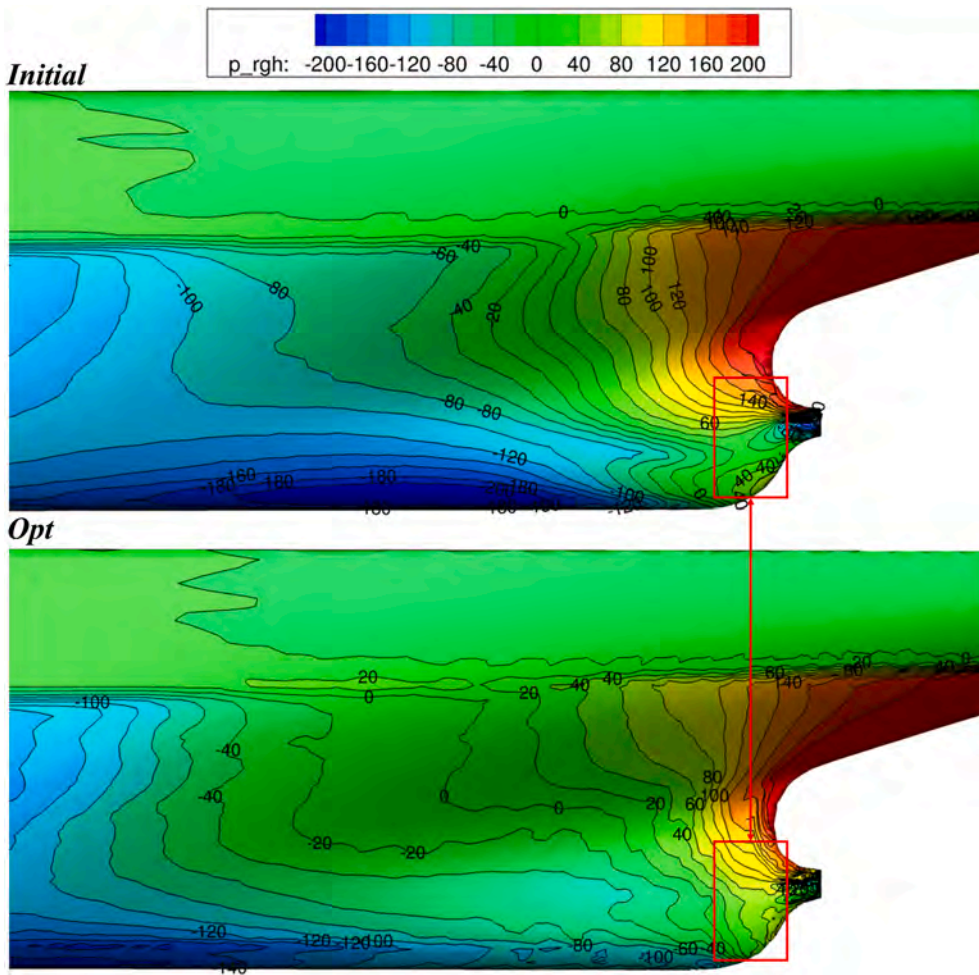p_rgh: -200-160-120 -80 -40  0  40  80 120 160 200

Opt

**Fig. 19.** The pressure comparison between the initial and optimized hull form.

s), $S$ is the wetted area.

For the propeller wake distortion optimization, the wake fraction is used to quantify the propeller wake distortion, which is defined as follows:

$$w = \frac{u}{V} = \frac{1}{N} \sum_{i=1}^{N} \frac{U^i}{V} \tag{28}$$

The $V$ denotes the velocity of the hull. $u$ is the average streamwise velocity at the propeller sampling plane. $N$ is the number of grid points on the propeller sampling plane, the $U^i$ are the velocity of grid points on the propeller sampling plane. Eq.(28) is equivalent to the usual wake fraction since the sampling points are distributed evenly inside a propeller disc. The radius of the sampling circle plane is 0.15 m and the center of the sampling circle plane is the center of the propeller shaft.
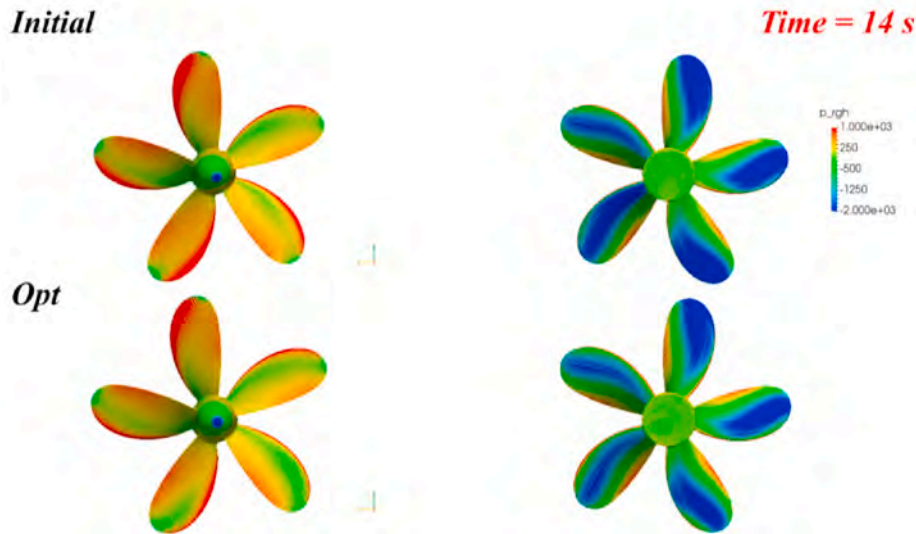
**Fig. 20.** The pressure distribution on the pressure side and suction side of the propeller.
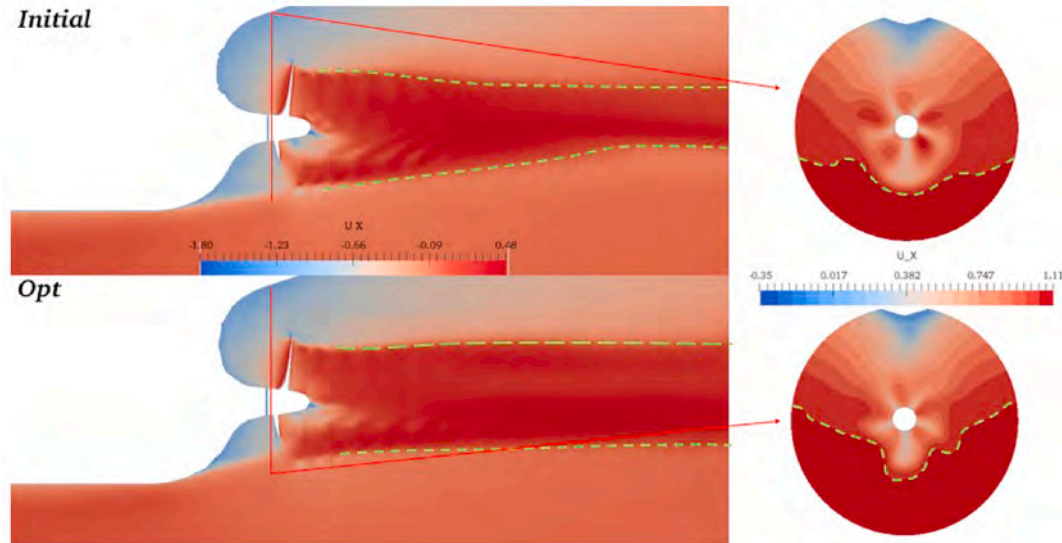


**Fig. 21.** The propeller wake comparison. The slice position is $x/L_{pp} = 0.9843$.

The propeller sampling plane is located at $x/L_{pp} = 0.9843$, shown as Fig. 13.

The multi-objective optimization problem for JBC hull can be described as follow:

Objective function 1: max (w) Objective function 2: min ($R_T$).

Subject to:

$\Delta V \leq 1.2\% V_{initial}$
$\Delta S \leq 0.6\% S_{initial}$
$B = B_{initial}$
$T = T_{initial} - 0.02 \leq X1 \leq 0.02 \ 0.05 \leq Y1 \leq 0.05 \ 0.03 \leq Y2 \leq -0.03$

NSGA-II is used to search the optimized hull for parameters and obtain the Pareto Front. We select an optimized point ($w = 0.36118$, $C_t = 0.004228$) to verify the optimization precision. The red point is shown in Fig. 14. The optimized deformation parameters are $X = 0.00444$ m, $Y1 = -0.04919$ m, $Y2 = -0.02995$ m.

### 3.6. Verification of optimization results

In this section, the precision of the multi-objective kriging model is verified using the cross-validation method(Miao and Wan, 2020b). In the cross-validation, 29 sampling points are selected in turn to construct a kriging model, and then the constructed kriging model was used to predict the hydrodynamic performance of the other point. This way aims to evaluate the accuracy and robustness of the kriging model. Fig. 15 shows that the kriging models have good stability and can be used for the optimization algorithm.

According to the optimized deformation parameters, the optimized hull form can be gotten utilizing the hull form deformation module. The optimized hull form is shown in Fig. 16. The bilge thickness of the optimized hull decreases and the V-shaped is formed. The $w$ of the initial JBC hull is 0.350, and the $C_t$ of the initial JBC hull is $4.630*10^{-3}$. The calculated $C_t$ of the optimized hull is 4.191*10-3, and the calculated $w$ of the optimized hull is 0.361. It demonstrates the JBC hull can obtain better hydrodynamic performances (such as resistance, wake fraction) utilizing the in-house hull form optimization software OPTShip-SJTU 2.1. The optimization comparisons are shown in Table 7.
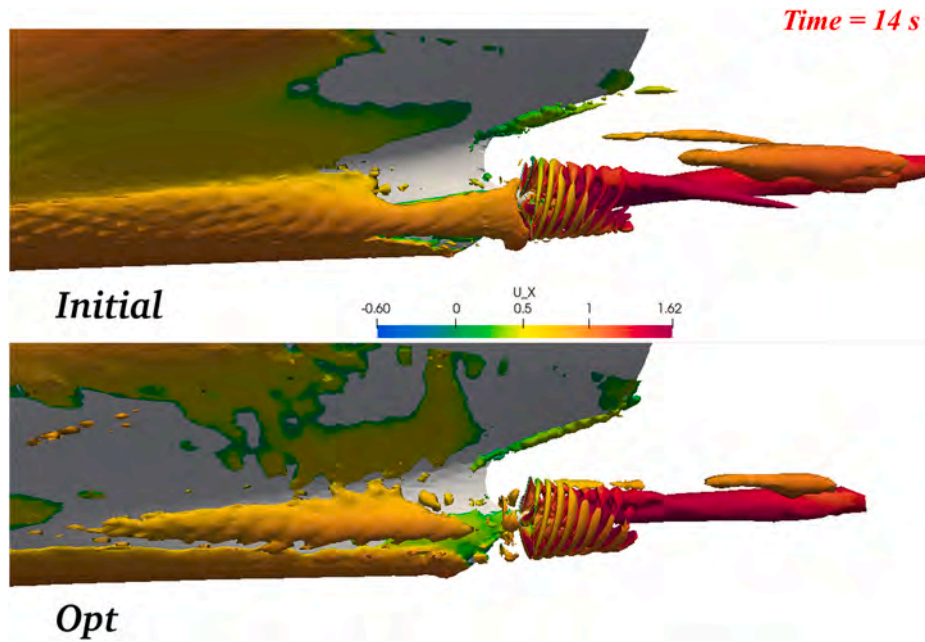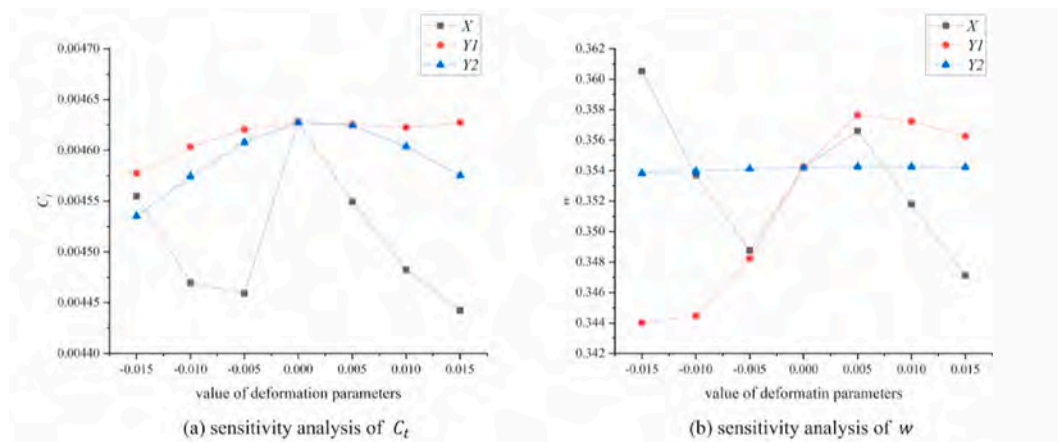
**Fig. 22.** The vortex comparison when the Q = 10.



**Fig. 23.** The sensitivity analysis of $C_t$ and.$w$

## 4. Results and discussions

### 4.1. Hull-propeller interaction analysis considering stern-shape

For the hull-propeller interaction optimization, firstly, the streamline is applied to display the flow field features, shown in Fig. 17. Compared with the initial hull form, the optimized hull form has a thin bilge. At the bilge of the initial hull form, the streamlines assemble at region 1 and region 2, which indicate there is flow bifurcation at the stern of the initial hull. Compared with the initial hull form, the streamlines of the optimized hull distribute more evenly at the bilge tube of the stern, which is beneficial for decreasing the inlet flow nonuniformity of the propeller. Considering Fig. 14, the modified stern shape can decrease the resistance and improve wake fraction simultaneously, and the objectives have a strong positive correlation under the deformation setting in this paper.

From Fig. 18, irregular shedding of the vortex structures may be existing at the propeller cap of the initial hull form, which leads to the flow disorder. The streamlines on the propeller surface of the optimized hull form are more orderly at the propeller hub. The flow field around the stern is optimized by modifying the stern shape, which achieves a better interaction between the hull and propeller.

Next, the pressure of the hull and propeller is shown in Fig. 19 and Fig. 20. The optimized hull form has a smoother stern ship compared with the initial hull form. The pressure contour space becomes larger and the change of pressure gradient becomes smoother than before. Therefore, the tiny fluctuations in the pressure contours are magnified. The pressure contours become wavy. The modified hull form changes the local flow field at the deformation region, which also results in wavy pressure contours. According to the pressure distribution on the hull surface at the stern, there exists a less intense adverse pressure gradient along the direction of the streamline on the optimized hull surface, which can delay the flow separation. The gradient of pressure around the stern surface changes smoother, which reduced the area of high-pressure and low-pressure. The area of pressure ($-40 = p \le 60$) becomes larger and the low-pressure ($p \le -100$) area becomes smaller. Overall, the pressure recovery is better than before and the total pressure resistance around the stern decreases. The pressure contour distribution affects the direction of flow, and the direction and distribution of streamlines of the optimized hull are more uniform than these of the initial hull form.

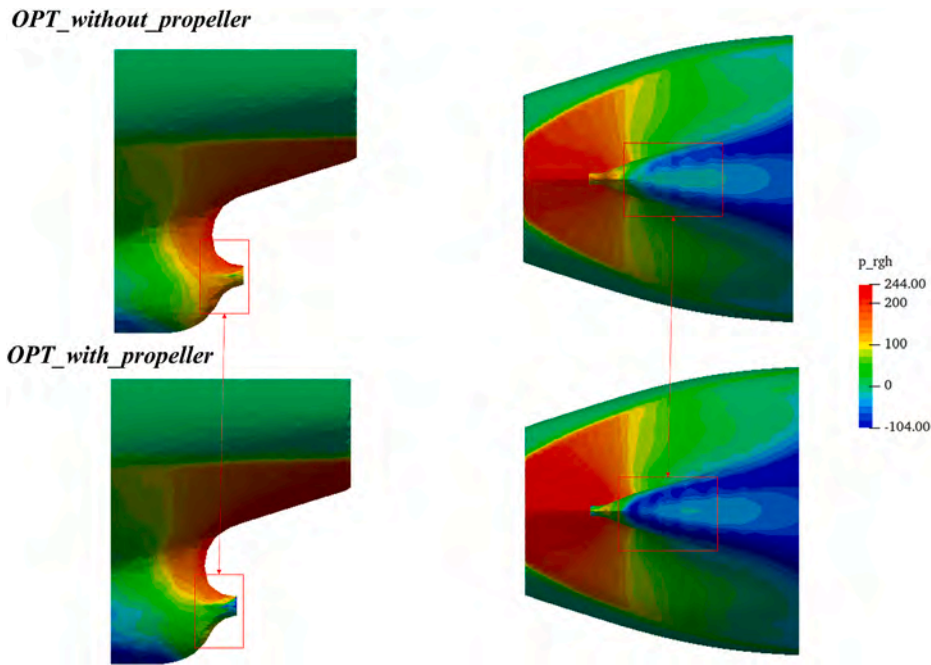Thrust is generated due to the pressure difference between the

**OPT_without_propeller**



**OPT_with_propeller**

**Fig. 24.** Comparison of the optimized hull form between without propeller and with propeller in pressure.

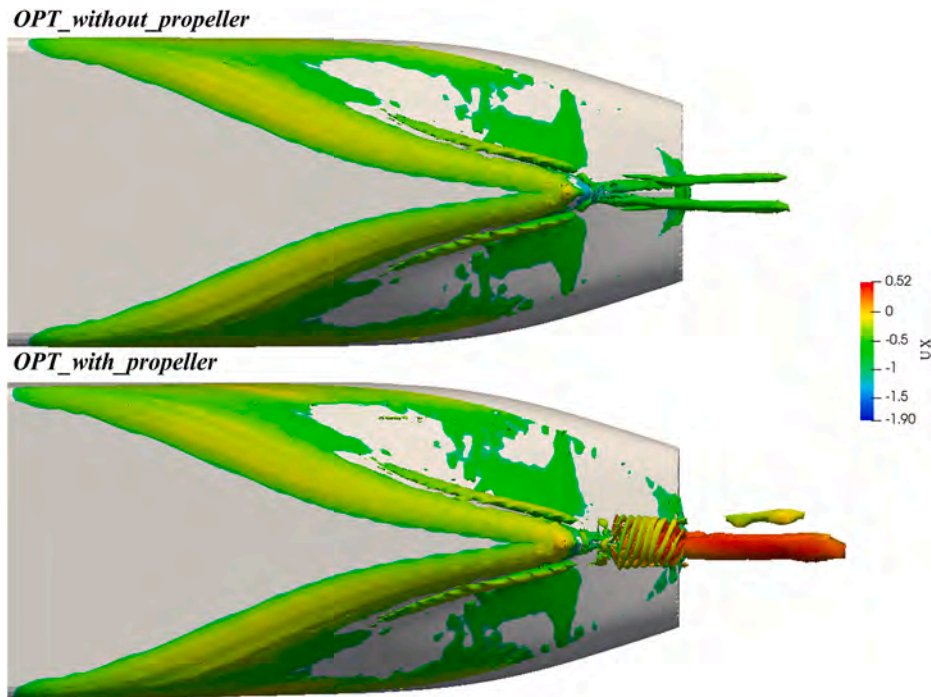**OPT_without_propeller**



**OPT_with_propeller**

**Fig. 25.** Comparison of the optimized hull form between with propeller and without propeller in Q = 10.

suction and pressure sides of the propeller. From Fig. 20, the low-pressure and high-pressure area of the propeller for the initial hull form is larger than the optimized hull form. It explains the optimized hull form has a lower thrust.

Compared with the initial hull form, the flow velocity direction of the optimized hull is nearly perpendicular to the propeller plane at the stern, which can improve the velocity uniformity at the propeller plane. From Fig. 21, the propeller wake of the optimized hull is steadier compared with the initial hull form. Because of the suction effect of the propeller, the flow near the bilge tube is accelerated, and flow separation is suppressed. The propeller wake is less disturbed by other flows and the velocity distortion is optimized. The wake faction of optimized hull form is 0.361 and improves by 3.14%.

Q criterion is used to extract the vortex distribution around the stern (Cao et al., 2021). A conclusion that can be gotten from the vortex distribution shown in Fig. 22 is the thinner bilge has a weak longitudinal vortex, which is more preferable for resistance reduction than the initial stern form (Duvigneau et al., 2003). The vortex distribution indicates flow intense, accordingly, there exists more smooth flow in the stern for the optimized hull. From Figs. 21 and 22, the vortex distribution of
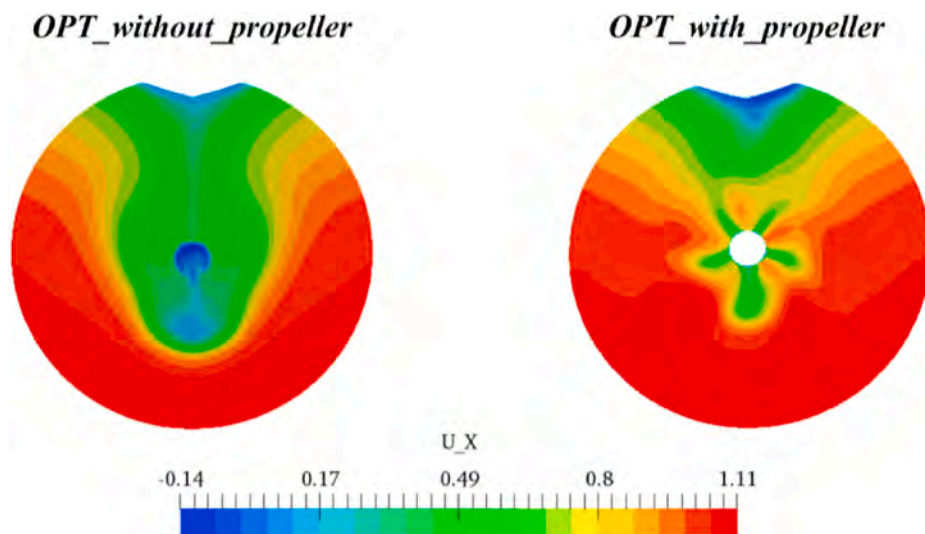
**Fig. 26.** Comparison of the optimized hull form between with propeller and without propeller in wake at $x/L_{pp} = 0.9843$.

propeller wake for initial hull form is more disperse, and the propeller wake flow field of optimized hull form is more orderly.

### 4.2. Parameters sensitivity and propeller effect analysis

The sensitivity analysis of $C_t$ and $w$ about deformation parameters are conducted utilizing the established multi-objective kriging surrogate model, shown in Fig. 23. In the aspect of $C_t$, the pattern between the deformation parameters *Y1, Y2,* and $C_t$ is clear. Because the *Y1* and *Y2* control the thickness of the stern, the thinner the hull stern shape, the lower the resistance. While the $C_t$ about *X* is irregular. The *X* controls the deformation of the stern along the x-direction at the third and fourth plane of the lattice, shown in Fig. 7. The deformation effect of *X* is less compared with the *Y1* and *Y2*. It has no direct influence on the $C_t$, and more studies should be conducted in the future. In the aspect of *w*, the *Y2* hardly affects the *w*. and a suitable value of *Y1* or *X* can improve the *w*.

For studying the impact of the propeller on the stern flow field, the hydrodynamic performances of the optimized hull form with propeller and without propeller are calculated. Fig. 24 shows the pressure distribution on the stern surface. In the red frame, the influences of the propeller are shown. Compared with the optimized hull form without a propeller, the high-pressure region is located above the stern shaft mainly. The pressure at the stern shaft decreases due to the propeller suction effect, and the negative pressure at the stern bottom increases. It leads to pressure resistance increasing. At the same time, flow velocity before the propeller increase under the propeller suction effect, which leads to the fraction resistance increasing. The thrust of the propeller isn't equal to the resistance of bare hull. Therefore, it is necessary to consider the propeller effect. The thrust deduction factor of optimized hull form with propeller is 0.163.

In the aspect of vortex construction distribution from Fig. 25, the difference in the distribution of the vortex structure at the stern is small between them. Affected by the rotation of the propeller, the shape of the vortex structure in the wake is quite different. The two vortex lines are merged into one vortex line by the propeller suction. From Fig. 26, the influence of propeller rotation is equally significant. It directly affects the velocity and pressure distribution of the wake flow field.

### 5. Summary

In this paper, the in-house hull form optimization software OPTShip-SJTU 2.1 is applied to optimize a model scale ship JBC with an actual propeller based on the dynamic overset grid method considering resistance and propeller wake simultaneously. Three hull form deformation

parameters are selected to control the shape of the stern based on the FFD method. Four months are taken to obtain the high-fidelity flow field information of different hull forms, including the propeller wake and total resistance. Finally, an optimized hull form is selected from the Pareto Front to analyze the relationship between the shape of the stern, hull flow field, and the propeller wake. The hydrodynamic performance of optimized hull form without propeller is calculated to investigate the influence of propeller preliminarily. The optimization results demonstrate the resistance decreases by 9.48% and the propeller wake performance increases by 3.14%. Several conclusions can be summarized as follows:

(1) There is a strong positive correlation between resistance and wake fraction under the deformation setting in this paper.
(2) For the full formed ship, contraction of hull line at the stern makes pressure gradient smoother than before, which changes the area of low-pressure and high-pressure. These reduce pressure resistance and make the propeller's incoming flow more uniform.
(3) The interaction flow optimization between the propeller and hull can be achieved utilizing the OPTShip-SJTU 2.1. A uniform and steady flow field can decrease the hull resistance and improve the wake fraction by modifying the stern shape in this paper. A lower thrust deduction can also be obtained.
(4) In an aspect of the propeller, the propeller rotation can change the pressure distribution and the vortex construction distribution in a small area. The propeller effect has a limited impact on the flow field before the propeller. While the shape of the stern has a large influence on the propeller performance. The propeller can increase the bare hull resistance by changing the pressure distribution. it is necessary to consider the propeller effect during the resistance and wake optimization.

In future work, the difference of optimization results between the bare hull and appended hull should be conducted to study the influence of the actual propeller further. Utilizing the hull-propeller interaction module, many complex optimization studies can be conducted, such as ship maneuvering optimization.

**Data availability**

The data that support the findings of this study are available from the corresponding author upon reasonable request.

**CRediT authorship contribution statement**

**Zhiqiang Liu:** Data curation, Writing – original draft, preparation, Visualization, Investigation, Software, Validation. **Weiwen Zhao:** Software, Data curation, Visualization, Investigation, Validation. **Decheng Wan:** Supervision, Conceptualization, Methodology, Investigation, Writing – review & editing.

**Declaration of competing interest**

The authors declare the following financial interests/personal relationships which may be considered as potential competing interests: Decheng Wan reports financial support was provided by Shanghai Jiao Tong University.

**Acknowledgements**

# References

Campana, E.F., Peri, D., Tahara, Y., Kandasamy, M., Stern, F., 2009. Numerical optimization methods for ship hydrodynamic design. Trans. Society Naval Architects Mar. Eng. 117, 30.

Cao, L.-s., Huang, F.-l., Liu, C., Wan, D.-c., 2021. Vortical structures and wakes of a sphere in homogeneous and density stratified fluid. J. Hydrodyn. 33 (2), 207–215. https://doi.org/10.1007/s42241-021-0032-x.

Chen, X., Diez, M., Kandasamy, M., Zhang, Z., Campana, E.F., Stern, F., 2015. High-fidelity global optimization of shape design by dimensionality reduction, metamodels and deterministic particle swarm. Eng. Optim. 47 (4), 473–494.

Deb, K., Pratap, A., Agarwal, S., Meyarivan, T., 2002. A fast and elitist multiobjective genetic algorithm: NSGA-II. IEEE Trans. Evol. Comput. 6 (2), 182–197.

Duvigneau, R., Visonneau, M., Deng, G.B., 2003. On the role played by turbulence closures in hull shape optimization at model and full scale. J. Mar. Sci. Technol. 8 (1), 11–25.

Feng, Y., Chen, Z., Dai, Y., Wang, F., Cai, J., Shen, Z., 2018. Multidisciplinary optimization of an offshore aquaculture vessel hull form based on the support vector regression surrogate model. Ocean Eng. 166, 145–158.

Ferrari, R., Froio, D., Rizzi, E., Gentile, C., Chatzi, E.N., 2019. Model updating of a historic concrete bridge by sensitivity-and global optimization-based Latin Hypercube Sampling. Eng. Struct. 179, 139–160.

Guo, J., Zhang, Y., Chen, Z., Feng, Y., 2020. CFD-based multi-objective optimization of a waterjet-propelled trimaran. Ocean Eng. 195, 106755. https://doi.org/10.1016/j.oceaneng.2019.106755.

He, P., Filip, G., Martins, J.R., Maki, K.J., 2019a. Design optimization for self-propulsion of a bulk carrier hull using a discrete adjoint method. Comput. Fluids 192, 104259.

He, P., Filip, G., Martins, J.R.R.A., Maki, K.J., 2019b. Design optimization for self-propulsion of a bulk carrier hull using a discrete adjoint method. Comput. Fluids 192. https://doi.org/10.1016/j.compfluid.2019.104259.

Hino, T., Stern, F., Larsson, L., Visonneau, M., Hirata, N., Kim, J., 2020. Numerical Ship Hydrodynamics: an Assessment of the Tokyo 2015 Workshop, 94. Springer Nature.

Hirata, N., Kobayashi, H., Hino, T., Toda, Y., Abdel-Maksoud, M., Stern, F., 2021. Experimental data for JBC resistance, sinkage, trim, self-propulsion factors, longitudinal wave cut and detailed flow with and without an energy saving circular duct. In: Hino, T., Stern, F., Larsson, L., Visonneau, M., Hirata, N., Kim, J. (Eds.), Numerical Ship Hydrodynamics: an Assessment of the Tokyo 2015 Workshop. Springer International Publishing, Cham, pp. 23–51.

Huang, F., Wang, L., Yang, C., 2015. Hull Form Optimization for Reduced Drag and Improved Seakeeping Using a Surrogate-Based Method. Paper Presented at the the Twenty-Fifth International Ocean and Polar Engineering Conference.

Ichinose, Y., Tahara, Y., 2018. A wake field design system utilizing a database analysis to enhance the performance of energy saving devices and propeller. J. Mar. Sci. Technol. 24 (4), 1119–1133. https://doi.org/10.1007/s00773-018-0611-x.

Kim, H., Yang, C., Jeong, S., Noblesse, F., 2011. Hull Form Design Exploration Based on Response Surface Method. Paper Presented at the the Twenty-First International Offshore and Polar Engineering Conference.

Kim, H., Yang, C., Noblesse, F., 2010. Hull Form Optimization for Reduced Resistance and Improved Seakeeping via Practical Designed-Oriented CFD Tools. Paper Presented at the Proceedings of the 2010 Conference on Grand Challenges in Modeling & Simulation.

Kinaci, O.K., Bayezit, I., Reyhanoglu, M., 2020. A practical feedforward speed control system for autonomous underwater vehicles. Ocean Eng. 218 https://doi.org/10.1016/j.oceaneng.2020.108214.

Li, J., Zhao, D., Wang, C., Sun, S., Ye, L., 2019. Method for the calculation of the underwater effective wake field for propeller optimization. Water 11 (1), 165. Retrieved from. https://www.mdpi.com/2073-4441/11/1/165.

Lin, Y., He, J., Li, K., 2018. Hull form design optimization of twin-skeg fishing vessel for minimum resistance based on surrogate model. Adv. Eng. Software 123, 38–50. https://doi.org/10.1016/j.advengsoft.2018.05.010.

Liu, X.-L., Chen, Y.-W., Jing, X.-R., Chen, Y.-G., 2011. Optimized Latin hypercube sampling method and its application. J. Natl. Univ. Def. Technol. 33 (5), 73–77.

Liu, X.-w., Chen, S.-t., Zhao, W.-w., Wan, D.-c., Wang, Y.-q., 2021. Liutex-based centripetal force field model for improving the resistance and wake performances of JBC ship sailing in calm water. J. Hydrodyn. 33 (3), 494–502. https://doi.org/10.1007/s42241-021-0046-4.

Liu, X., Wan, D., Chen, G., Hu, C., 2019. Wigley Hull Form Optimization with or without Bulbous Bow. Paper Presented at the the 29th International Ocean and Polar Engineering Conference.

Liu, Z., Liu, W., Chen, Q., Luo, F., Zhai, S., 2020. Resistance reduction technology research of high speed ships based on a new type of bow appendage. Ocean Eng. 206, 107246. https://doi.org/10.1016/j.oceaneng.2020.107246.

Liu, Z., Liu, X., Wan, D., 2020. Wigley Hull Design Optimization Based on Artificial Neural Network and Genetic Algorithm. Paper Presented at the the Fourteenth ISOPE Pacific/Asia Offshore Mechanics Symposium.

Menter, F.R., Kuntz, M., Langtry, R., 2003. Ten years of industrial experience with the SST turbulence model. Heat Mass Tran. 4.

Miao, A., Wan, D., 2020a. CFD-based multi-objective optimisation of S60 Catamaran considering Demihull shape and separation. Appl. Ocean Res. 97, 102071. https://doi.org/10.1016/j.apor.2020.102071.

Miao, A., Wan, D., 2020b. Hull form optimization based on an NM+CFD integrated method for KCS. Int. J. Comput. Methods 17 (10). https://doi.org/10.1142/s0219876220500085.

Noack, R., Boger, D., Kunz, R.e., Carrica, P., 2009. Suggar++: an improved general overset grid assembly capability. In: 19th AIAA Computational Fluid Dynamics, p. 3992.

Park, J.-H., Choi, J.-E., Chun, H.-H., 2015. Hull-form optimization of KSUEZMAX to enhance resistance performance. Int. J. Naval Architect. Ocean Eng. 7 (1), 100–114. https://doi.org/10.1515/ijnaoe-2015-0008.

Ren, Z., Wang, J., Wan, D., 2020. Investigation of the flow field of a ship in planar motion mechanism tests by the vortex identification method. J. Mar. Sci. Eng. 8 (9), 649.

Roache, P.J., 1998. Verification and Validation in Computational Science and Engineering, 895. Hermosa Albuquerque, NM.

Sederberg, T.W., Parry, S.R., 1986. Free-form Deformation of Solid Geometric Models. Paper Presented at the Proceedings of the 13th Annual Conference on Computer Graphics and Interactive Techniques.

Shen, Z., Wan, D., Carrica, P.M., 2015. Dynamic overset grids in OpenFOAM with application to KCS self-propulsion and maneuvering. Ocean Eng. 108, 287–306.

Stern, F., Wilson, R., Shao, J., 2006. Quantitative V&V of CFD simulations and certification of CFD codes. Int. J. Numer. Methods Fluid. 50 (11), 1335–1355.

Sun, S., Zhao, X., 2019. RANS based calm water resistance prediction for Tumblehome hull with different bow appendages. https://doi.org/10.1115/OMAE2019-95449.

Tahara, Y., Peri, D., Campana, E.F., Stern, F., 2011. Single-and multiobjective design optimization of a fast multihull ship: numerical and experimental results. J. Mar. Sci. Technol. 16 (4), 412–433.

Wang, J., Zhao, W., Wan, D., 2016. Free Maneuvering Simulation of ONR Tumblehome Using Overset Grid Method in Naoe-FOAM-SJTU Solver. Paper Presented at the 31th Symposium on. Naval Hydrodynamics, Monterey, USA.

Wang, J., Zou, L., Wan, D., 2018. Numerical simulations of zigzag maneuver of free running ship in waves by RANS-Overset grid method. Ocean Eng. 162, 55–79.

Wang, Y., Gao, T., Pang, Y., Tang, Y., 2019. Investigation and optimization of appendage influence on the hydrodynamic performance of AUVs. J. Mar. Sci. Technol. 24 (1), 297–305. https://doi.org/10.1007/s00773-018-0558-y.

Wu, J., Liu, X., Wan, D., 2016. Multi-Objective Hydrodynamic Optimization of Ship Hull Based on Approximation Model. Paper Presented at the the 26th International Ocean and Polar Engineering Conference.

Yang, C., Huang, F., Hyunyul, K., 2015. Hydrodynamic optimization of a triswach. J. Hydrodyn. Ser. B 26 (6), 856–864.

Yu, J.-W., Lee, C.-M., Lee, I., Choi, J.-E., 2017. Bow hull-form optimization in waves of a 66,000 DWT bulk carrier. Int. J. Naval Architect. Ocean Eng. 9 (5), 499–508. https://doi.org/10.1016/j.ijnaoe.2017.01.006.

Zhang, S., Zhang, B., Tezdogan, T., Xu, L., Lai, Y., 2018. Computational fluid dynamics-based hull form optimization using approximation method. Eng. Appl Comput. Fluid Mech. 12 (1), 74–88. https://doi.org/10.1080/19942060.2017.1343751.

Zhu, Q.-d., Ma, Y., 2019. A design of T-foil and trim tab for fast catamaran based on NSGA-II. J. Hydrodyn. 32 (1), 161–174. https://doi.org/10.1007/s42241-019-0055-8.